



Multi-scavenging functional separator ensuring the cycling stability of high energy density lithium-ion batteries

Da-Ae Lim ^a , Jin-Hong Seok ^a, Seong-Jae Lim ^b, Dong-Won Kim ^{a,b,*} 

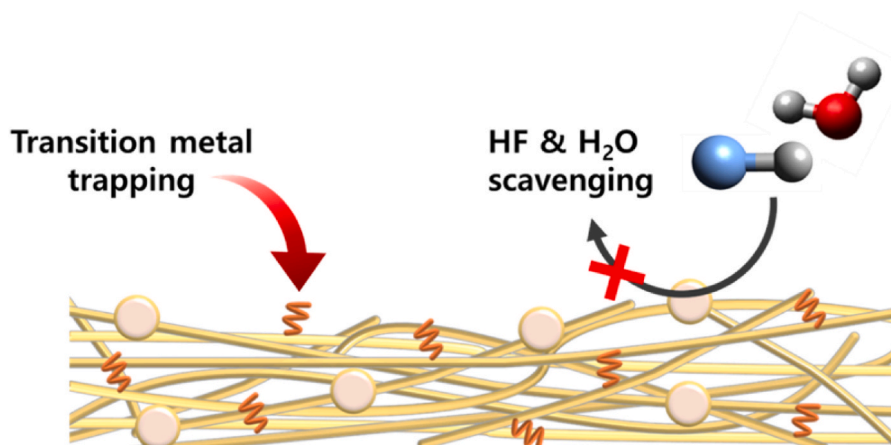
^a Department of Chemical Engineering, Hanyang University, Seoul, 04763, Republic of Korea

^b Department of Battery Engineering, Hanyang University, Seoul, 04763, Republic of Korea

HIGHLIGHTS

- A multi-scavenging separator was prepared with PAN, zeolite and polyethyleneimine.
- The separator mitigated electrode and electrolyte degradation by capturing impurities.
- The cell employing multi-scavenging separator exhibited superior cycling performance.

GRAPHICAL ABSTRACT



ARTICLE INFO

Keywords:

Lithium-ion battery
Ni-rich cathode
Impurity scavenger
Functional separator
High-temperature performance

ABSTRACT

Ni-rich $\text{LiNi}_x\text{Co}_y\text{Mn}_{1-x-y}\text{O}_2$ (NCM) materials are key cathode active materials for achieving high energy densities in lithium-ion batteries (LIBs). However, their practical applications are hindered by interfacial and structural instabilities such as microcracking, transition metal dissolution, and oxidative decomposition of the electrolyte at the cathode surface, which cause an increase in cell resistance and performance degradation. These problems are exacerbated by the parasitic reactions of impurities, such as H_2O , HF, and transition metals during cycling. In this study, we fabricate a grafted polyacrylonitrile membrane containing zeolite (GPANZ) as a multi-scavenging functional separator to improve LIB cycling performance. GPANZ consists of H_2O - and HF-removing functional zeolite and a transition-metal-chelate functional polyethyleneimine, thus effectively capturing various impurities in the cell. Therefore, the GPANZ separator can mitigate electrode and electrolyte degradation by suppressing the deleterious effects of impurities. The graphite/ $\text{LiNi}_{0.8}\text{Co}_{0.1}\text{Mn}_{0.1}\text{O}_2$ cell with the GPANZ separator exhibits superior cycling performance in terms of discharge capacity, cycle life, and rate performance,

* Corresponding author. Department of Chemical Engineering, Hanyang University, Seoul, 04763, Republic of Korea.

E-mail address: dongwonkim@hanyang.ac.kr (D.-W. Kim).

<https://doi.org/10.1016/j.jpowsour.2025.237016>

Received 6 March 2025; Received in revised form 1 April 2025; Accepted 7 April 2025

Available online 10 April 2025

0378-7753/© 2025 Elsevier B.V. All rights reserved, including those for text and data mining, AI training, and similar technologies.

especially at high temperatures. Our work highlights the necessity of removing impurities to ensure battery performance and provides new insights for designing functional separators for LIBs.

1. Introduction

Lithium-ion batteries (LIBs) have become an indispensable part of sustainable energy storage devices in electric vehicles and other storage systems, owing to their long life and high energy density [1–3]. Ni-rich $\text{LiNi}_x\text{Co}_y\text{Mn}_{1-x-y}\text{O}_2$ (NCM) cathodes with high specific capacities and operating voltages have emerged as key components of high energy density LIBs. However, these Ni-rich NCM materials suffer from electrolyte decomposition at the cathode surface owing to the highly reactive Ni^{4+} , intergranular cracking, and structural deterioration, such as the formation of inactive rock-salt phases and cation mixing [4–9]. These deteriorations are accelerated in LiPF_6 -based electrolytes and are prone to generating highly corrosive HF by LiPF_6 hydrolysis. Corrosive HF etches the cathode surface, damaging the cathode–electrolyte interphase (CEI) and dissolving the transition metal (TM), leading to battery performance degradation [10–12]. The dissolved TM is shuttled and reduced on the anode surface, causing solid electrolyte interphase (SEI) destruction and electrolyte reduction, thus promoting the formation of a resistive SEI that hinders Li^+ intercalation into the graphite anode [13–15].

To address these issues, removing impurities (H_2O , HF, and TM) from the electrolyte is key to achieving high battery performance. Several efforts have been made to capture impurities through chemical and physical interactions. Electrolyte additives containing Lewis basic sites, such as phosphite, amino silane (Si-N), and isocyanate moieties, have been employed to chemically scavenge H_2O [16–18]. Xu et al. used a dicyano-functionalized additive as a moisture scavenger to enhance the thermal and cycling stabilities of graphite/NCM cells [19]. Additionally, HF can be scavenged by complexation with additives that impart basic electron-donating groups, such as trimethylsilyl, phosphite, Si-O, and Si-N [20–22]. Kim et al. reported improved cycle life and structural stability for graphite/NCM cell by the addition of 3-(trimethylsilyl)-2-oxazolidinone [23]. The use of porous materials such as zeolites and metal–oxide frameworks (MOFs) was also considered a promising strategy for capturing H_2O and HF [24–26]. These materials exhibit porous structures with abundant absorption sites and high H_2O absorption capabilities. HF can be removed via chemical reactions with the zeolite skeleton or through functional groups on the MOF surface [27,28]. Additionally, TM trapping using metal-chelating groups based on nitrogen compounds, such as amines, imines, and edetates, has been conducted [29,30]. These groups generally possess non-bonded lone pair electrons on nitrogen atoms that can coordinate bonds with target metal ions, enabling effective capture of TMs [31]. As a further strategy, recent research has focused on incorporating functional materials into the separator to suppress electrode degradation and mitigate cross-talk effects originating from the counter electrode [32]. However, research on the simultaneous scavenging of multiple types of impurities is limited.

In this study, we present a grafted polyacrylonitrile membrane containing zeolite (GPANZ) as a multi-scavenging functional separator to scavenge impurities and mitigate LIB degradation. GPANZ was fabricated by electrospinning a zeolite-containing polyacrylonitrile and grafting a polyethyleneimine (PEI) moiety onto the membrane. Zeolite can scavenge H_2O and HF, and the $-\text{NH}_2$ groups in PEI can absorb TM. Thus, the GPANZ membrane could effectively prevent electrode and electrolyte deterioration induced by impurities, thereby enhancing the cycling stability of LIBs. The unique properties of GPANZ for capturing impurities were characterized using nuclear magnetic resonance (NMR) spectroscopy, Karl Fischer titration, inductively coupled plasma-mass spectrometry (ICP-MS), and X-ray photoelectron spectroscopy (XPS). A graphite/ $\text{LiNi}_{0.8}\text{Co}_{0.1}\text{Mn}_{0.1}\text{O}_2$ (NCM811) cell assembled with a GPANZ

separator improved cycling performance by alleviating the adverse effects of impurity-driven cell failure, especially at elevated temperatures. The enhanced cycling characteristics and structural stability of the cell employing GPANZ separator were investigated using electrochemical impedance spectroscopy (EIS), scanning electron microscopy (SEM), transmission electron microscopy (TEM), and time-of-flight secondary ion mass spectrometry (TOF-SIMS).

2. Experimental section

2.1. Materials

PAN (Mw = 150,000), branched-polyethyleneimine (b-PEI, Mw = 25,000), N,N-dimethylformamide (DMF), and ethylene glycol were purchased from Sigma-Aldrich and used as received. Zeolite (ZSM-5) was obtained from Acros Organics and used without further treatment. A polyethylene (PE) separator (ND420, Ashai) with a thickness of 20 μm was used after vacuum drying at 60 °C for 12 h. A liquid electrolyte containing 1.15 M lithium hexafluorophosphate (LiPF_6) in a mixed solution of ethylene carbonate, ethyl methyl carbonate, and diethyl carbonate (3:5:2 v/v) with 5.0 wt% fluoroethylene carbonate was kindly supplied by Dongwha Electrolyte Co. Ltd.

2.2. Preparation of GPANZ

The GPANZ separator was prepared via electrospinning and grafting. PAN membrane with zeolites (PANZ) was prepared by electrospinning. PAN (10 wt%) was dissolved in DMF and agitated at 60 °C for 8 h. After cooling the solution to room temperature, 2 wt% zeolite was added to the polymer solution and ball milled for 12 h. The mixed solution was then loaded into a plastic syringe with a 21-gauge needle, and a tip-to-collector distance of 15 cm was maintained. A high voltage of 17 kV was applied with a feed rate of 1.0 mL h^{-1} for 40 min. The obtained PANZ was peeled from the collector and vacuum dried at 80 °C for 12 h to remove any remaining DMF. To fabricate GPANZ, 60 mg of the electrospun PANZ membrane was added to 50 mL of a mixture of b-PEI and ethylene glycol (10 mg b-PEI per 1 mL ethylene glycol). The reaction mixture was refluxed with vigorous stirring at 140 °C for 4 h. When the reaction was complete, the obtained GPANZ was filtered, sequentially washed with deionized water and ethanol several times, and then vacuum dried for 12 h at 80 °C.

2.3. Lithium-ion cell assembly

The NCM811 cathode was coated onto an aluminum current collector with a slurry composed of NCM811 (Umicore), poly(vinylidene fluoride) (PVdF, Solvay), and Super P (TIMCAL) with a mass ratio of 95:3:2. A graphite anode was fabricated by casting a slurry containing graphite (BTR), PVdF, and Super P (91:8:1 by mass) onto a copper foil. In the cathode, the mass loading was measured to be 14.0 mg cm^{-2} , corresponding to an areal capacity of 2.8 mAh cm^{-2} . Meanwhile, the graphite anode showed a mass loading of 9.8 mg cm^{-2} with an areal capacity of 3.3 mAh cm^{-2} . The 2032-type coin cells were assembled with a graphite anode, different separators (PE, PANZ, GPANZ), 50 μL of liquid electrolyte, and an NCM811 cathode. All cells were fabricated in a high-purity Ar-filled glovebox with H_2O and O_2 concentrations of <1.0 ppm.

2.4. Electrochemical measurements

Ionic conductivities at different temperatures were measured using

EIS in the frequency range of 10 Hz to 1 MHz (CHI660d, CH Instruments). The transference number of lithium ions (t_{Li^+}) was measured in a symmetrical lithium cell using AC impedance and DC polarization [33]. The graphite/NCM811 cell was galvanostatically cycled using a battery tester (WBCS3000, WonATech) in the voltage range of 2.5–4.3 V at 25 and 55 °C. Before cycling, two preconditioning cycles were performed at a 0.1 C rate. The cell was then subjected to galvanostatic charge and discharge cycles at a current density of 1.0 C. After the constant-current charging step in each cycle, constant-voltage charging was performed until the current reached 0.05 C. Cell rate performance was evaluated by charging the cell at the same current rate (0.2 C) and discharging it at different current rates. EIS of the cell during cycling was performed using an electrochemical workstation (CHI660d, CH Instruments) in the frequency range of 1 mHz–1 MHz at an amplitude of 5 mV.

2.5. Characterization

Separator and electrode morphologies were examined by field-emission scanning electron microscopy (FE-SEM; Verios G4UC, FEI). Fourier-transform infrared (FTIR) spectroscopy was conducted to confirm the chemical composition of materials using a Nicolet iS50 spectrometer in the wavenumber range of 400–4000 cm^{-1} . Thermal shrinkage of the separator was determined from dimensional changes after keeping the separator at different temperatures for 1 h. The contact angle between the electrolyte droplet and the separator was measured using a contact angle analyzer (Phoenix300, SEO). The porosity of membrane was measured using n-butanol impregnation [34]. To investigate the HF scavenging ability of the separator, electrolytes were treated with 300 ppm water and different separators, and stored at 55 °C for 3 days. Subsequently, the ^{19}F NMR spectra (VNMRS 600 MHz, Agilent Technologies) were recorded. Hexafluoro benzene (1 wt%, C_6F_6 , Sigma Aldrich) was added to tetrahydrofuran- d_8 (THF- d_8 , Cambridge Isotope Laboratories, Inc.) and used as an internal reference for the ^{19}F NMR spectra. TM dissolution and deposition were quantitatively analyzed using ICP-MS (iCAP RQ, Thermo Fisher Scientific). The electrode surface chemical composition was investigated using XPS (K-Alpha, Thermo Fisher Scientific) under an ultrahigh vacuum. The phase transitions of the cycled NCM811 cathodes were investigated using high-resolution transmission electron microscopy (HR-TEM, JEOL 2100F). Time-of-flight secondary-ion mass spectrometry (TOF-SIMS,

TOF-SIMS 5, and ION TOF) was performed after cycling to analyze the surface and bulk chemical compositions of the electrodes.

3. Results and discussion

Fig. 1a shows a schematic of the GPANZ preparation. The PANZ membrane was first fabricated by electrospinning a mixture of PAN and zeolite, which was then reacted with the b-PEI solution to graft the PEI moiety onto the PAN membrane. Nitrile groups ($\text{C}\equiv\text{N}$) in PAN initiated the reaction with amine groups ($-\text{NH}_2$) in PEI, forming the amidine ($\text{N}-\text{C}=\text{N}$) and amide groups ($\text{C}=\text{O}-\text{NH}$), as shown in Fig. S1 [35]. After PEI grafting, the obtained GPANZ exhibited a homogeneous yellow color and high flexibility (Fig. 1b and Fig. S2). Fig. 1c illustrates the multi-functional characteristics of GPANZ separators. Embedded zeolites can effectively scavenge H_2O and HF, thereby preventing electrode and electrolyte deterioration during cycling [25,27]. Additionally, the amine groups in b-PEI possess electron-donating properties that can trap TM, thereby blocking its shuttling and the graphite anode degradation [31].

Fig. 2a and b shows the FE-SEM and optical images of GPANZ, respectively. SEM images reveal that zeolite particles were uniformly embedded within the nanofibers with an average diameter of 700 nm, and the thickness of the free-standing GPANZ separator was 25 μm (Fig. 2b). FTIR spectra of PANZ and GPANZ were obtained to confirm the chemical structure of GPANZ (Fig. 2c). In the GPANZ spectrum, a strong $\text{C}\equiv\text{N}$ peak in PANZ at 2242 cm^{-1} decreased, and four peaks at 1224, 1569, 1626, and 3000–3600 cm^{-1} , corresponding to $\text{C}-\text{N}$, $\text{N}-\text{H}$, $-\text{C}=\text{O}/-\text{C}=\text{N}$, and $-\text{NH}$ adsorption, respectively, were observed. This result indicates that $\text{C}\equiv\text{N}$ groups in PANZ are converted to $\text{N}-\text{C}=\text{N}$ and $\text{C}=\text{O}-\text{NH}$ groups after the grafting reaction, as depicted in Fig. S1. The thermal stabilities of the PE and GPANZ separators were compared after storage at different temperatures for 1 h (Fig. 2d). The PE separator underwent severe shrinkage at 140 °C owing to PE melting, while the GPANZ separator hardly shrank at the same temperature due to its high thermal stability. The GPANZ separator maintained thermal stability up to 200 °C and exhibited only minimal shrinkage even at an elevated temperature of 250 °C, as presented in Fig. S3. The physical properties of the PE and GPANZ separators are summarized in Table S1. The GPANZ separator comprising nanofibers exhibited higher porosity and electrolyte uptake than the PE separator. Contact angles were measured by dropping liquid electrolytes onto the two separators. As depicted in Fig. 2e, the contact angle of GPANZ was 18.4°, which was much smaller

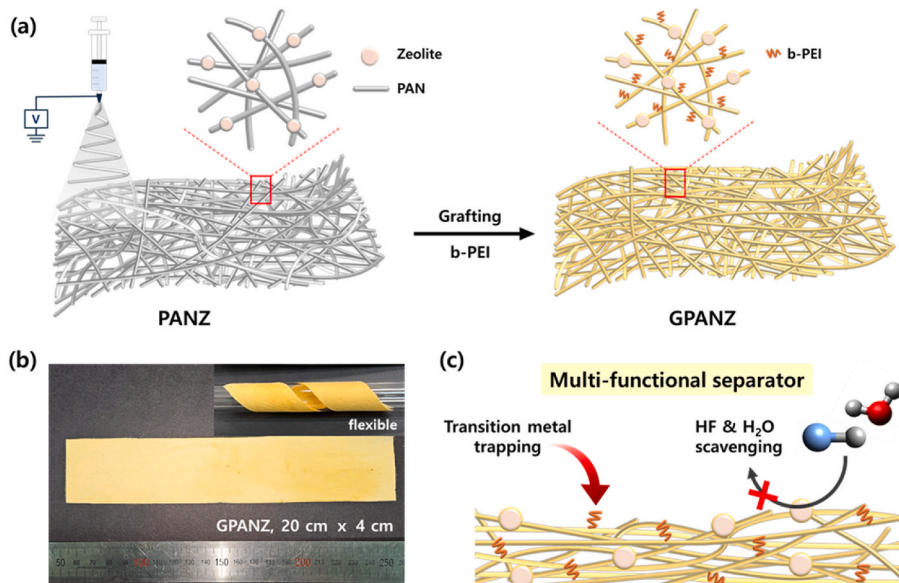


Fig. 1. (a) Schematic for preparing GPANZ. (b) Large-sized GPANZ separator and its flexibility. (c) Schematic showing the multiple functions of the GPANZ separator.

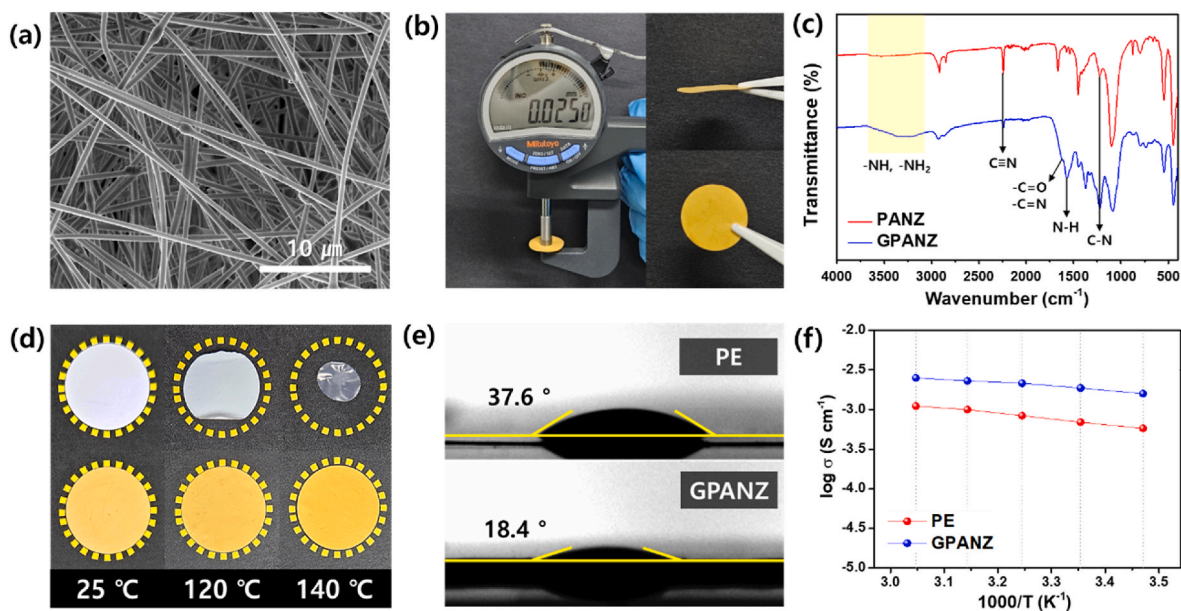


Fig. 2. (a) SEM image and (b) photograph of the fibrous GPANZ separator. (c) FTIR spectra of PANZ and GPANZ. Comparison of (d) thermal shrinkage at different temperatures and the (e) contact angles of the two separators. (f) Ionic conductivities of the PE and GPANZ separators soaked with liquid electrolyte as a function of temperature.

than that of the PE separator (37.6°). Fig. S4 presents the stress–strain curves of the GPANZ separator before and after immersion in liquid electrolyte. The mechanical properties remained unchanged after soaking, indicating that the GPANZ separator exhibits negligible swelling in liquid electrolytes. The ionic conductivities of the different separators soaked in liquid electrolyte were measured using EIS, and their temperature dependences are shown in Fig. 2f. The ionic conductivities of GPANZ are higher than those of the PE separator over all temperature ranges, which can be ascribed to the higher porosity and electrolyte uptake of GPANZ. The transference number of the Li^+ ions (t_{Li^+}) was determined by combining DC polarization and AC impedance spectroscopy (Fig. S5). GPANZ had a higher t_{Li^+} value (0.43) than PE (0.29), which can be attributed to the high lithium-ion dissociation ability of functional groups (amine and nitrile) and hydrogen bonding for trapping anions in GPANZ separator [36,37].

LiPF_6 , which is used as a salt in LIBs, thermally decomposes into LiF and PF_5 . PF_5 reacts with trace amounts of water to produce highly reactive and corrosive HF, and these reactions are accelerated at high temperatures. The produced HF causes parasitic side reactions and damages the interphase (CEI, SEI) and structure of the electrodes, which leads to the dissolution and deposition of TM ions, thereby degrading battery performance (Fig. 3a). Subsequent deterioration occurs continuously because of additional water produced by these reactions [11,38]. Therefore, suppressing the generation of H_2O and HF in the electrolyte is essential for improving battery performance at high temperatures. To investigate the H_2O scavenging ability of the GPANZ separator, Karl Fischer titration measurements were conducted with different electrolytes. The H_2O content of the fresh electrolyte was 5 ppm, and it was increased to 219 ppm by intentionally adding a small amount of water. After treating H_2O -added electrolyte with GPANZ for 24 h, the H_2O content decreased dramatically from 219 to 47 ppm (Fig. 3b), suggesting that the zeolite embedded in the GPANZ separator effectively captured residual H_2O in the electrolyte. To confirm the role of GPANZ as an HF scavenger, ^{19}F NMR analysis of the liquid electrolytes treated with PE and GPANZ separators was conducted. The PE and GPANZ separators were immersed in the electrolyte with a membrane-to-electrolyte volume ratio of 0.05. To investigate the HF scavenging effect, H_2O (300 ppm) was added into the electrolyte solutions with PE and GPANZ, and the electrolytes were stored at 55°C for 3 days. Without any treatment,

the fresh electrolyte shows three peaks at -75.0 , -124.3 , and -164.9 ppm corresponding to PF_6^- , FEC, and C_6F_6 (internal reference), respectively (Fig. 3c) [39,40]. After storing the water-adding electrolyte with the PE separator at 55°C , a new small broad peak corresponding to HF appeared at -191.1 ppm (Fig. 3d), indicating that HF was formed by the autocatalytic decomposition of LiPF_6 and H_2O . In contrast, no noticeable HF peak is observed for the electrolyte treated with GPANZ, as depicted in Fig. 3e. These results suggest that the GPANZ separator can act as an effective H_2O and HF scavenger to prevent battery performance degradation.

The electrochemical performance of the graphite/NCM811 cells with different separators was evaluated at 25 and 55°C . Voltage profiles and cycling characteristics of the cells with different separators at 25°C and 1 C are presented in Figs. S6 and 4a, and 4b. The GPANZ cell delivered a higher initial discharge capacity of 185.4 mAh g^{-1} and showed a better capacity retention of 80.5 % after 500 cycles compared to the PE separator cell (180.1 mAh g^{-1} , 71.6 %). Figs. S7 and 4c show the charge–discharge curves of the cells with PE and GPANZ at 55°C and 1 C. The GPANZ cell initially delivered a higher discharge capacity of 186.1 mAh g^{-1} than that of the PE cell (182.6 mAh g^{-1}). Similar to the cycling performance observed at 25°C , the GPANZ cell exhibited an enhanced capacity retention (64.3 %) after 500 cycles compared to that of the PE cell (42.2 %) at 55°C (Fig. 4d). Furthermore, the GPANZ cell showed superior cycling performance compared to the PANZ cell, which can be attributed to the TM-scavenging ability of PEI that enhances cycling stability. Notably, a significant difference in Coulombic efficiency was evident between the cells tested at 55°C . Elevated temperatures promote unfavorable processes, such as oxidative decomposition of the electrolyte and degradation of the SEI layer, which in turn increase irreversible losses during cycling. As a result, the PE-based cell exhibited lower Coulombic efficiency at 55°C . To investigate the effect of the separator on cell rate performance, a rate capability test was conducted at a constant charge rate of 0.2 C and various discharge C rates from 0.2 to 5.0 C. Fig. S8 shows the first discharge curves of cells assembled with PE and GPANZ at each C rate, and discharge capacities at different C rates are compared in Fig. 4e. The GPANZ cell exhibits higher discharge capacities than the PE cell at all C rates because of the high ionic conductivity and Li^+ transference number of the GPANZ separator, as discussed previously. AC impedance spectra of graphite/

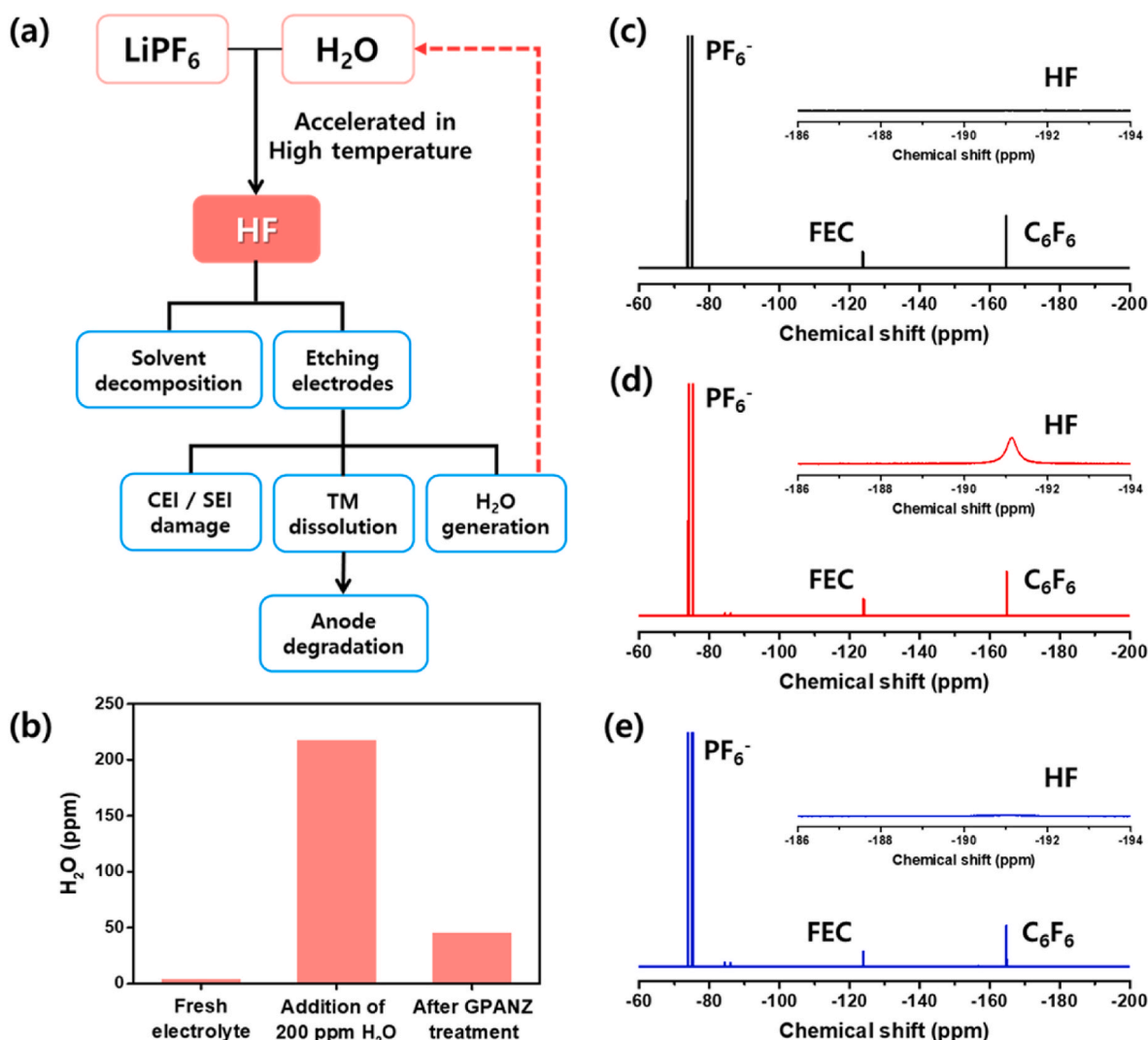


Fig. 3. (a) Deterioration mechanisms of LIBs due to residual water and HF formation in the cell. (b) H_2O scavenging ability of GPANZ. ^{19}F NMR spectra of (c) the fresh electrolyte, (d) the electrolyte with H_2O and PE stored at 55°C for 3 days, and (e) the electrolyte with H_2O and GPANZ stored at 55°C for 3 days.

NCM811 cells employing different separators were obtained to monitor internal resistances of cells during cycling at 55°C . In these spectra (Fig. 4f and g), there are two overlapping semicircles in the high- and low-frequency regions, corresponding to ion migration at the surface film on the electrode (R_f) and the charge-transfer reaction at the electrode-electrolyte interface (R_{ct}) [41,42]. The obtained spectra could be fitted to the equivalent circuit shown in Fig. S9, and the fitting results are listed in Table S2. The GPANZ cell exhibited slightly smaller initial resistances than the PE cell because of the superior electrochemical properties of GPANZ. Furthermore, increases in both electrolyte (R_e) and interfacial resistance ($R_f + R_{ct}$) of the GPANZ cell were slower than those of the PE cell during cycling. As mentioned earlier, GPANZ effectively removed impurities (H_2O and HF) in the cell, suppressing electrolyte and electrode material deterioration, thereby mitigating the increase in the internal resistance of the cell.

Fig. 5a illustrates the beneficial effect of the GPANZ separator in the cell employing the LiPF_6 -based electrolyte in terms of stabilizing the interfacial layer and the electrode structure. During cycling, the corrosive HF arising from the thermal decomposition and hydrolysis of LiPF_6 etches the electrodes and their interphases (CEI and SEI), resulting in bilateral degradation of the cathode and anode. On the cathode side, the TM dissolution and the damage of CEI formed on the cathode active material are caused by HF attack, leading to the deterioration of NCM

material and oxidative decomposition of the electrolyte. The dissolved TM was reduced at the graphite anode, impairing the SEI and promoting electrolyte decomposition, thereby constructing a thick and resistive SEI layer on the graphite anode. These processes increase cell resistance and eventually lead to cell failure [11,14]. However, the GPANZ separator effectively mitigated cell degradation by suppressing impurity (H_2O , HF , and TM) generation and capturing them. The role of GPANZ in inhibiting TM dissolution from the cathode and trapping it was evaluated using ICP-MS by quantifying the contents of the dissolved and deposited TM. To measure the TM content dissolved from the NCM cathode, the cathode was fully charged to 4.3 V after pre-cycling and then immersed in electrolytes with different separators at 55°C for 3 days. The results are summarized in Table S3. When the cathode was stored in the electrolyte with the PE separator, the amounts of Ni, Co, and Mn were measured to be 20.3, 2.6, and 1.7 ppm, respectively. While TM contents decreased to 12.0, 1.3, and 0.9 ppm, respectively, in the electrolyte containing the GPANZ separator. In terms of separator type, the TM content decreased in the order of PE > PANZ > GPANZ, which supports the effectiveness of PEI grafting onto PANZ in minimizing TM dissolution, likely due to its strong electron-donating properties. These results highlight the effectiveness of the GPANZ separator in mitigating HF -induced corrosion and stabilizing the cathode-electrolyte interphases. ICP-MS results of the graphite anode retrieved from cells

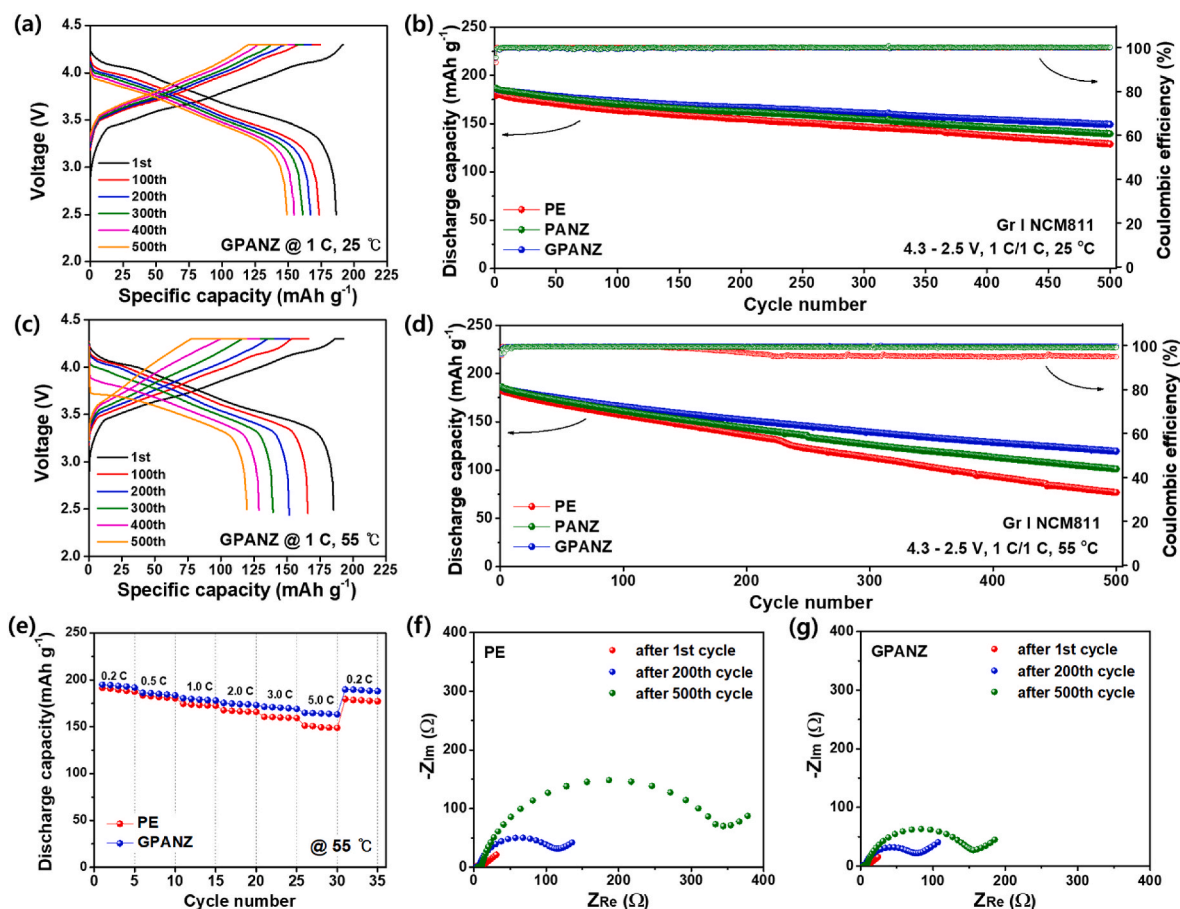


Fig. 4. Voltage profiles of the GPANZ cell at (a) 25 °C and (c) 55 °C (1.0 C rate). Cycling performance of the graphite/NCM811 cells assembled with different separators at (b) 25 °C and (d) 55 °C (1.0 C rate). (e) Discharge capacities of the cells with different separators as a function of C rate at 55 °C. Nyquist plots for the first, 200th, and 500th cycles of the cells assembled with (f) PE and (g) GPANZ separators at 55 °C.

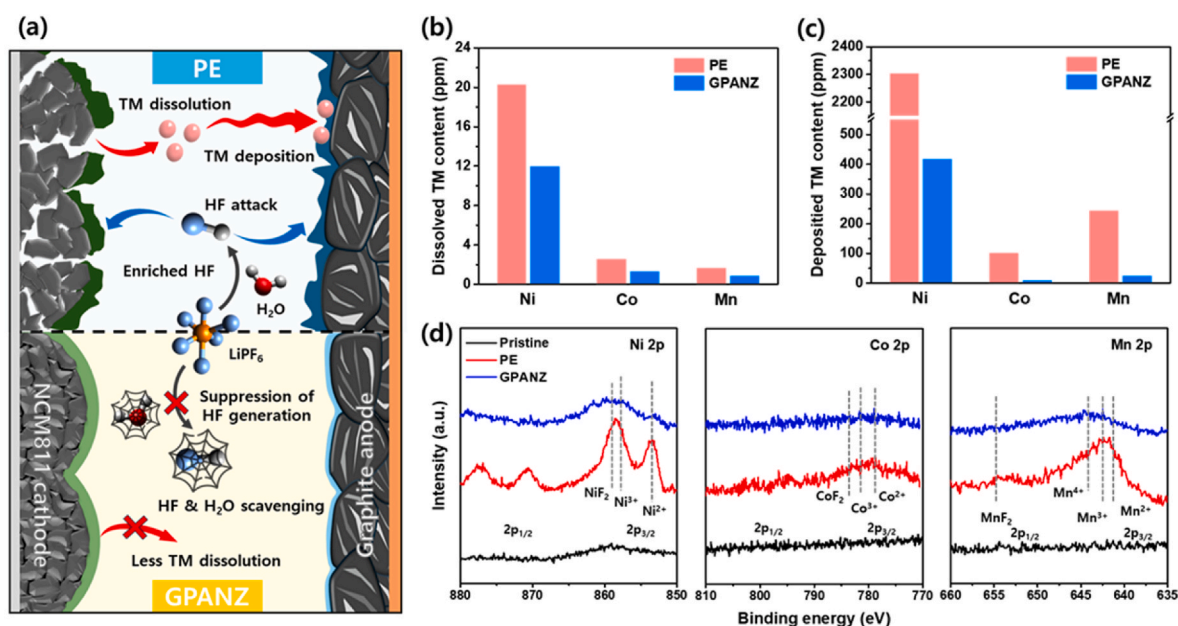


Fig. 5. (a) Schematic of the effectiveness of GPANZ separator for mitigating cell degradation. (b) Contents of TMs dissolved in the electrolyte after contacting the fully charged NCM811 cathode with PE and GPANZ at 55 °C for 3 days. (c) Contents of TMs deposited onto the graphite anode with PE and GPANZ separators after 300 cycles at 55 °C. (d) XPS spectra (Ni 2p, Co 2p, Mn 2p) of the surface elements on the pristine and graphite anodes cycled with different separators.

assembled with different separators after 300 cycles at 55 °C were obtained to quantify the TM content deposited onto the anode. As presented in Fig. 5c, severe TM deposition occurred in the graphite anode cycled with PE separator, resulting in the presence of Ni, Co, and Mn at concentrations of 2304.5, 102.6, and 245.3 ppm, respectively. In contrast, TM deposition on the graphite anode was significantly reduced when applying the GPANZ separator (418.4, 11.4, and 25.6 ppm for Ni, Co, and Mn, respectively). To further clarify the suppressive effect of the GPANZ separator on the shuttling and deposition of TM species, XPS spectra of the graphite anodes cycled at elevated temperatures were obtained (Fig. 5d). For the graphite cycled with the PE separator, the obvious peaks of Ni, Co, and Mn species were observed, whereas no clear spectral features of these TMs appeared in the spectra of the graphite cycled with the GPANZ separator. These ICP-MS and XPS results revealed that the GPANZ separator mitigated TM leaching from delithiated NCM cathode and the deposition of shuttled TM on the graphite anode during cycling.

Cross-sectional morphologies of the cathodes cycled with different separators were examined using FE-SEM. (Fig. 6a–6f). Notably, the structural stability of the NCM cathode differed remarkably when different separators were used. The NCM cathode cycled with the PE separator exhibited large volume expansion and contained some microcracks in the NCM secondary particles (Fig. 6b and e). In the PE separator cell, the HF generated during cycling etches the cathode surface, and continuous side reactions occur between the electrolyte and

the newly exposed cathode surface, resulting in the formation of a non-uniform and resistive CEI. This CEI leads to an inhomogeneous lithiation process and severe anisotropic volume change, accelerating the structural degradation of the NCM cathode [43–46]. Conversely, thickening and intergranular cracking of the cathode material were remarkably suppressed in the cell with the GPANZ separator (Fig. 6c and f). The microstructure of NCM cathodes was investigated using HR-TEM and fast Fourier transform (FFT) after 300 cycles at 55 °C (Fig. 6g and h). At the NCM cathode surface, the highly reactive Ni^{4+} was reduced to lower oxidation states (Ni^{3+} and Ni^{2+}) by anodic decomposition of the electrolyte during the charging process. Ni^{2+} easily migrates into vacant Li slabs, causing undesirable Ni/Li cation mixing and the formation of a rock-salt phase. The inactive rock-salt phase impedes Li-ion transport in the layered structure of the cathode, thereby losing the Li storage capability [47]. Fig. 6g shows that the surface of the NCM cathode cycled with the PE separator was composed of a rock-salt phase and a thick-mixed phase (rock-salt + layered), with a total phase transformation thickness of 19.2 nm. In contrast, the GPANZ separator drastically reduces the phase transition region to 8.9 nm at the cathode surface, as shown in Fig. 6h. This result can be ascribed to the HF suppression effect of GPANZ, which mitigates the exposure of the active cathode surface to the liquid electrolyte.

The TOF-SIMS depth profile of the cycled NCM in Fig. S10 shows the chemical composition of the cathode surface. Strong PO_3^- and weak Ni^- signals were detected in the NCM cycled with the PE separator, which

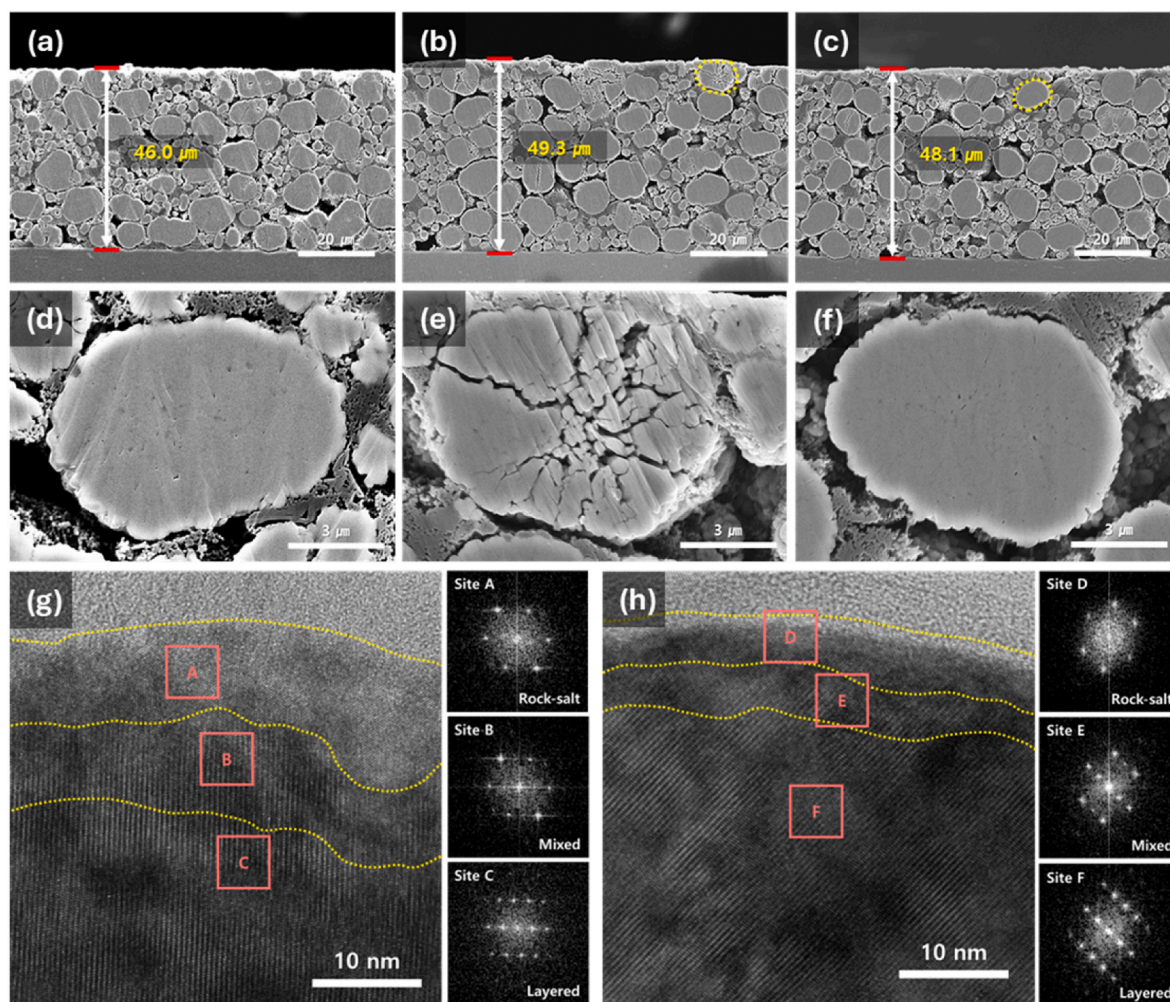


Fig. 6. Cross-sectional SEM image of the pristine NCM811 cathode (a, d). Cross-sectional SEM images of the NCM811 cathodes after 300 cycles at 55 °C with (b, e) PE separator and (c, f) GPANZ separator. HR-TEM images with their FFT patterns of NCM811 cathodes retrieved from the cells with (g) PE separator and (h) GPANZ separator after 300 cycles at 55 °C.

were ascribed to the decomposition product of LiPF₆ at the cathode [48, 49]. In contrast, the NCM cathode cycled with the GPANZ separator was covered with a thin electrolyte decomposition layer with smaller PO₃⁻ signals, indicating that less electrolyte decomposition occurred. These results demonstrate that the GPANZ separator effectively alleviates structural degradation of the NCM cathode and the decomposition of the electrolyte at the cathode surface. TOF-SIMS analysis of the graphite anode was also performed to confirm the contribution of GPANZ to the interfacial stability of the anode. As shown in Fig. 7a and b, the graphite anode cycled with the PE separator exhibited a strong PO₃⁻ signal and a weaker graphite (C₆⁻) signal, indicating that overgrown SEI was formed by electrolyte decomposition catalyzed from TM and HF. Conversely, in the presence of the GPANZ separator, a relatively thin SEI was formed, implying that GPANZ suppressed electrolyte decomposition at the anode surface. Surface TM element mapping of the graphite anodes after 300

cycles was performed to further clarify the deposition of TM (Fig. 7c and d). The graphite anode cycled with the PE separator showed strong TM (Ni⁺, Co⁺, and Mn⁺) signals, whereas there were no apparent TM signals on the graphite anode cycled with the GPANZ separator. The decrease in TM deposition can be attributed to the impurity suppression ability of GPANZ, as previously discussed. The cross-sectional SEM images of the graphite anodes in the fully discharged state showed that the cycled graphite anode with the GPANZ separator had a lower volume expansion of 107.8 % than the anode with the PE separator (114.2 %) (Fig. S11). When using the GPANZ separator, electrode thickening can be mitigated by inhibiting the accumulation of byproducts generated from electrolyte decomposition. Thus, our results demonstrate that the multi-scavenging functional separator, GPANZ, can significantly improve the cycling performance of LIBs at elevated temperatures.

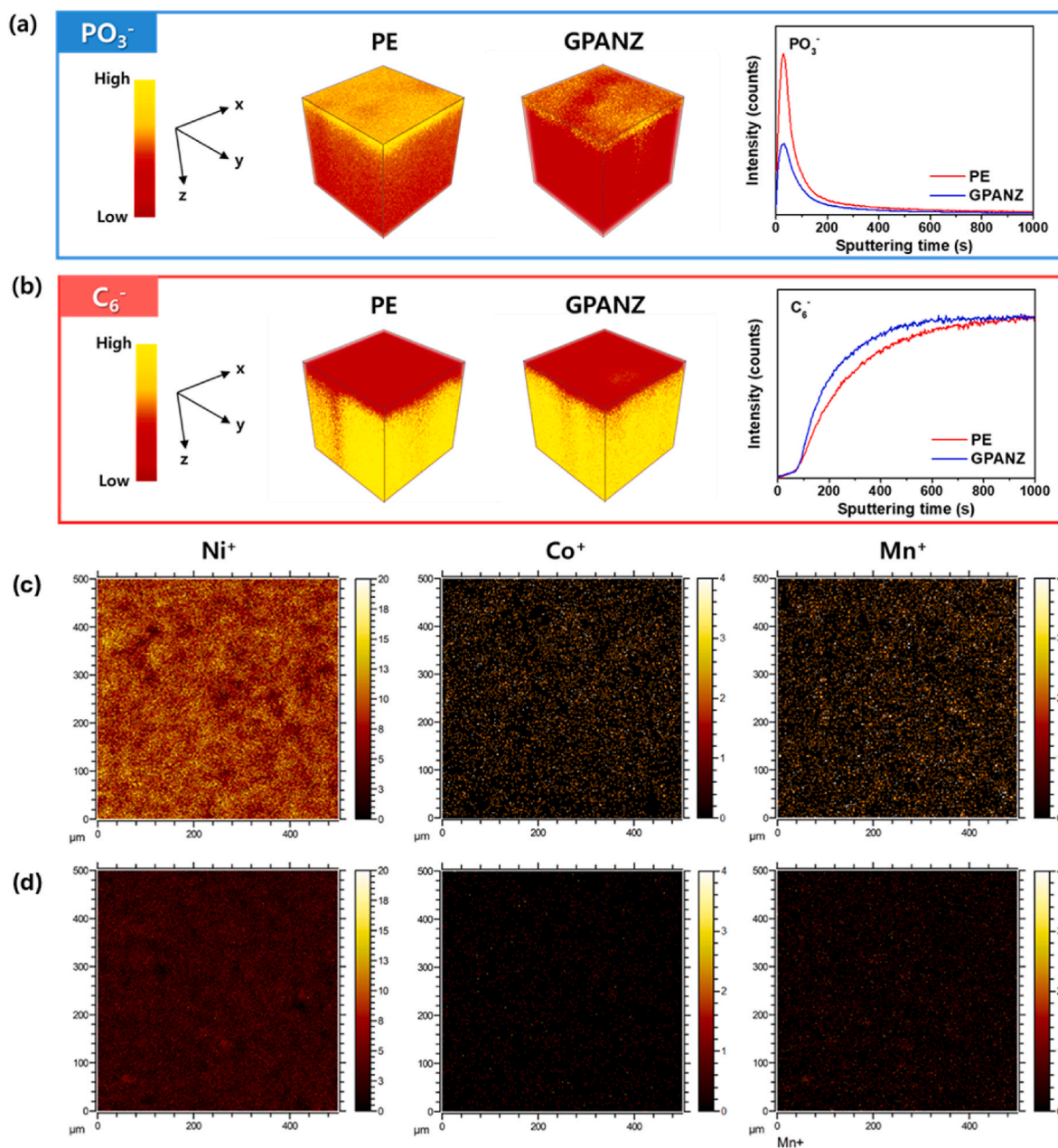


Fig. 7. TOF-SIMS analysis of graphite anodes obtained from the graphite/NCM811 cells assembled with different separators after 300 cycles at 55 °C. 3D TOF-SIMS depth images and profiles for (a) PO₃⁻ and (b) C₆⁻ ions. Surface TOF-SIMS spectra for Ni⁺, Co⁺, and Mn⁺ ions on graphite anodes cycled with (c) PE and (d) GPANZ separators.

4. Conclusions

In this study, we prepared a multi-impurity scavenging separator, GPANZ, and applied it to the graphite/NCM811 cell to enhance its cycling performance. The GPANZ consisted of zeolite-embedded PAN nanofibers with PEI moiety and was fabricated using electrospinning and grafting PEI. The embedded zeolite functioned as an H₂O and HF scavenger, and the amine groups in the PEI effectively trapped TMs; thus, the GPANZ separator effectively prevented impurity-induced deterioration of the electrodes and electrolytes. Additionally, the GPANZ separator exhibited superior electrochemical properties and enhanced thermal stability compared to the conventional PE separator at high temperatures. Consequently, the graphite/NCM811 cell assembled with the GPANZ separator delivered a high initial discharge capacity of 186.1 mAh g⁻¹ and exhibited enhanced cycle life with a capacity retention of 64.3 % after 500 cycles at 1 C rate and 55 °C. Our results revealed that the use of a GPANZ separator is a promising way to ensure cycling stability for high-capacity LIBs, especially at elevated temperatures.

CRediT authorship contribution statement

Da-Ae Lim: Writing – original draft, Investigation, Data curation, Conceptualization. **Jin-Hong Seok:** Methodology, Formal analysis. **Seong-Jae Lim:** Validation, Methodology. **Dong-Won Kim:** Writing – review & editing, Supervision, Project administration, Funding acquisition, Conceptualization.

Declaration of competing interest

The authors declare that they have no known competing financial interests or personal relationships that could have appeared to influence the work reported in this paper.

Acknowledgments

This study was financially supported by the Choi Research Foundation of Korea (NRF) grant funded by the Korean government (MSIT) (RS-2024-00454354) and the HRD Program for Industrial Innovation (RS-2024-00417730).

Appendix A. Supplementary data

Supplementary data to this article can be found online at <https://doi.org/10.1016/j.jpowsour.2025.237016>.

Data availability

Data will be made available on request.

References

- [1] F. Duffner, N. Kronmeyer, J. Tubke, J. Leker, M. Winter, R. Schmuch, Post-lithium-ion battery cell production and its compatibility with lithium-ion cell production infrastructure, *Nat. Energy* 6 (2021) 123–134, <https://doi.org/10.1038/s41560-020-00748-8>.
- [2] J.W. Choi, D. Aurbach, Promise and reality of post-lithium-ion batteries with high energy densities, *Nat. Rev. Mater.* 1 (2016) 16013, <https://doi.org/10.1038/natrevmats.2016.13>.
- [3] S. Chu, Y. Cui, N. Liu, The path towards sustainable energy, *Nat. Mater.* 16 (2017) 16–22, <https://doi.org/10.1038/nmat4834>.
- [4] W. Li, E.M. Ericson, A. Manthiram, High-nickel layered oxide cathodes for lithium-based automotive batteries, *Nat. Energy* 5 (2021) 26–34, <https://doi.org/10.1038/s41560-019-0513-0>.
- [5] X. Zeng, C. Zhan, J. Lu, K. Amine, Stabilization of a high-capacity and high-power nickel-based cathode for Li-Ion batteries, *Chem* 4 (2018) 690–704, <https://doi.org/10.1016/j.chempr.2017.12.027>.
- [6] S.-T. Myung, F. Maglia, K.-J. Park, C.S. Yoon, P. Lamp, S.-J. Kim, Y.-K. Sun, Nickel-rich layered cathode materials for automotive lithium-ion batteries: achievements and perspectives, *ACS Energy Lett.* 2 (2017) 196–223, <https://doi.org/10.1021/acsenerylett.6b00594>.
- [7] W. Liu, P. Oh, X. Liu, M.J. Lee, W. Cho, S. Chae, Y. Kim, J. Cho, Nickel-rich layered lithium transition-metal oxide for high-energy lithium-ion batteries, *Angew. Chem. Int. Ed.* 54 (2015) 4440–4457, <https://doi.org/10.1002/anie.201409262>.
- [8] S.S. Zhang, Problems and their origins of Ni-rich layered oxide cathode materials, *Energy Storage Mater.* 24 (2020) 247–254, <https://doi.org/10.1016/j.ensm.2019.08.013>.
- [9] M. Jiang, D.L. Danilow, R.-A. Eichel, P.H.H. Notten, A review of degradation mechanisms and recent achievements for Ni-rich cathode-based Li-Ion batteries, *Adv. Energy Mater.* 11 (2021) 2103005, <https://doi.org/10.1002/aenm.202103005>.
- [10] K. Xu, Electrolytes and interphases in Li-Ion batteries and beyond, *Chem. Rev.* 114 (2014) 11503, <https://doi.org/10.1021/cr500003w>.
- [11] K. Kim, H. Ma, S. Park, N.-S. Choi, Electrolyte-additive-driven interfacial engineering for high-capacity electrodes in lithium-ion batteries: promise and challenges, *ACS Energy Lett.* 5 (2020) 1537–1553, <https://doi.org/10.1021/acsenerylett.0c00468>.
- [12] J. Liu, M. Yue, S. Wang, Y. Zhao, J. Zhang, A review of performance attenuation and mitigation strategies of lithium-ion batteries, *Adv. Funct. Mater.* 32 (2022) 2107769, <https://doi.org/10.1002/adfm.202107769>.
- [13] D.-S. Ko, J.-H. Park, S. Park, Y.N. Ham, S.J. Ahn, J.-H. Park, H.N. Han, E. Lee, W. S. Jeon, C. Jung, Microstructural visualization of compositional changes induced by transition metal dissolution in Ni-rich layered cathode materials by high-resolution particle analysis, *Nano Energy* 56 (2019) 434–442, <https://doi.org/10.1016/j.nanoen.2018.11.046>.
- [14] C. Zhan, T. Wu, J. Lu, K. Amine, Dissolution, migration, and deposition of transition metal ions in Li-ion batteries exemplified by Mn-based cathodes – a critical review, *Energy Environ. Sci.* 11 (2018) 243–257, <https://doi.org/10.1039/C7EE03122J>.
- [15] H. Xu, Z. Li, T. Liu, C. Han, C. Guo, H. Zhao, Q. Li, J. Lu, K. Amine, X. Qiu, Impacts of dissolved Ni²⁺ on the solid electrolyte interphase on a graphite anode, *Angew. Chem. Int. Ed.* 134 (2022) e202202894, <https://doi.org/10.1002/anie.202202894>.
- [16] X. Zeng, C. Zhan, J. Lu, K. Amine, Lifetime limit of tris(trimethylsilyl) phosphite as electrolyte additive for high voltage lithium ion batteries, *RSC Adv.* 6 (2016) 38342–38349, <https://doi.org/10.1039/C6RA06555D>.
- [17] A.S. Wotango, W.-N. Su, E.G. Leggesse, A.M. Haregewoin, M.-H. Lin, T.A. Zegeye, Ju-H. Cheng, B.-J. Hwang, Improved interfacial properties of MCM6 electrode by 1-(Trimethylsilyl)imidazole as new electrolyte additive to suppress LiPF₆ decomposition, *ACS Appl. Mater. Interfaces* 9 (2017) 2410–2420, <https://doi.org/10.1021/acsami.6b13105>.
- [18] S.S. Zhang, Aromatic isocyanate as a new type of electrolyte additive for the improved performance of Li-ion batteries, *J. Power Sources* 163 (2006) 567–572, <https://doi.org/10.1016/j.jpowsour.2006.09.046>.
- [19] C. Xu, S. Renault, M. Ebadi, Z. Wang, E. Bjorklund, D. Guyomard, D. Brandell, K. Destrom, T. Gustafsson, LiTfD: a highly efficient additive for electrolyte stabilization in lithium-ion batteries, *Chem. Mater.* 29 (2017) 2254–2263, <https://doi.org/10.1021/acs.chemmater.6b05247>.
- [20] J.-G. Han, K. Kim, Y. Lee, N.-S. Choi, Scavenging materials to stabilize LiPF₆-Containing carbonate-based electrolytes for Li-Ion batteries, *Adv. Mater.* 31 (2019) 1804822, <https://doi.org/10.1002/adma.201804822>.
- [21] Y. Li, Q. Qu, L. Lv, J. Shao, H. Zheng, A multifunctional additive capable of electrolyte stabilization and structure/interphases regulation of high-energy Li-ion batteries, *Adv. Funct. Mater.* 34 (2024) 2314100, <https://doi.org/10.1002/adfm.202314100>.
- [22] B. Deng, H. Wang, W. Ge, X. Li, X. Yan, T. Chen, M. Qu, G. Peng, Investigating the influence of high temperatures on the cycling stability of a LiNi_{0.6}Co_{0.2}Mn_{0.2}O₂ cathode using an innovative electrolyte additive, *Electrochim. Acta* 236 (2017) 61–71, <https://doi.org/10.1016/j.electacta.2017.03.155>.
- [23] K. Kim, D. Hwang, S. Kim, S. O. Park, H. Cha, Y.-S. Lee, J. Cho, S.K. Kwak, N.-S. Choi, Cyclic aminosilane-based additive ensuring stable electrode–electrolyte interfaces in Li-Ion batteries, *Adv. Energy Mater.* 10 (2020) 2000012, <https://doi.org/10.1002/aenm.202000012>.
- [24] A.U. Mu, G. Cai, Z. Chen, Metal–organic frameworks for the enhancement of lithium-based batteries: a mini review on emerging functional designs, *Adv. Sci.* 11 (2024) 2305280, <https://doi.org/10.1002/advs.202305280>.
- [25] S. Maiti, H. Sclar, X. Wu, J. Grinblat, M. Talianker, A. Kondrakow, B. Markovsky, C. Aurbach, Zeolites as multifunctional additives stabilize high-voltage Li-batteries based on LiNi_{0.5}Mn_{1.5}O₄ cathodes, mechanistic studies, *Energy Storage Mater.* 56 (2023) 25–39, <https://doi.org/10.1016/j.ensm.2023.01.004>.
- [26] Q. Hu, G. Han, A. Wang, K. Gao, J. Liao, M. Ding, Y. Zhou, R. Dominko, H. Wang, J. Yao, Functionalized MOF enables stable cycling of nickel-rich layered oxides for lithium-ion batteries, *Chem. Eng. J.* 497 (2024) 154608, <https://doi.org/10.1016/j.cej.2024.154608>.
- [27] J. Xu, X. Xiao, S. Zeng, M. Cai, M.W. Verbrugge, Multifunctional lithium-ion-exchanged zeolite-coated separator for lithium-ion batteries, *ACS Appl. Energy Mater.* 1 (2018) 7237–7243, <https://doi.org/10.1021/acsaem.8b01716>.
- [28] H.B. Son, J. Cho, K. Baek, J. Jung, S. Nam, D.-Y. Han, S.J. Kang, H.R. Moon, S. Park, All-impurities scavenging, safe separators with functional metal-organic-frameworks for high-energy-density Li-Ion battery, *Adv. Funct. Mater.* 33 (2023) 2302563, <https://doi.org/10.1002/adfm.202302563>.
- [29] C. Zou, Y. Huang, L. Zhao, W. Ren, Z. Zhao, J. Liu, X. Li, M. Wang, B. Guo, Y. Lin, Mn²⁺ ions capture and uniform composite electrodes with PEI aqueous binder for advanced LiMn₂O₄-Based battery, *ACS Appl. Mater. Interfaces* 14 (2022) 14226–14234, <https://doi.org/10.1021/acsaami.2c00392>.

- [30] A. Banerjee, B. Ziv, S. Luski, D. Aurbach, I.C. Halalay, Increasing the durability of Li-ion batteries by means of manganese ion trapping materials with nitrogen functionalities, *J. Power Sources* 341 (2017) 457–465, <https://doi.org/10.1016/j.jpowsour.2016.12.036>.
- [31] W. Gao, M.R. Razanajatovo, Y. Song, X. Zhao, Z. Zhao, Q. Peng, T. Jiao, X. Liu, Q. Zhang, Efficient heavy metal sequestration from water by Mussel-inspired polystyrene conjugated with polyethyleneimine, *Chem. Eng. J.* 429 (2022) 132599, <https://doi.org/10.1016/j.cej.2021.132599>.
- [32] B. Ge, L. Hu, X. Yu, L. Wang, C. Fernandez, N. Yang, Q. Liang, Q.-H. Yang, Engineering triple-phase interfaces around the anode toward practical alkali metal–air batteries, *Adv. Mater.* 36 (2024) 2400937, <https://doi.org/10.1002/adma.202400937>.
- [33] P.G. Bruce, J. Evans, C.A. Vincent, Conductivity and transference number measurements on polymer electrolytes, *Solid State Ionics* 28–30 (1988) 918–922, [https://doi.org/10.1016/0167-2738\(88\)90304-9](https://doi.org/10.1016/0167-2738(88)90304-9).
- [34] Y. Dou, S. Wang, M.E. Gilbril, F. Kong, Electrospun of polyvinyl alcohol composite hydrogel nanofibers prepared by in-situ polymerization: a novel approach to fabricate hydrogel nanofiber membrane for lithium-ion batteries, *Chem. Eng. J.* 481 (2024) 148435, <https://doi.org/10.1016/j.cej.2023.148435>.
- [35] Y.A.Y.A. Mohammed, A.M. Abdel-Mohsen, Q.-J. Zhang, M. Younas, L.-B. Zhong, J.-C.E. Yang, Y.-M. Zheng, Facile synthesis of ZIF-8 incorporated electrospun PAN/PEI nanofibrous composite membrane for efficient Cr(VI) adsorption from water, *Chem. Eng. J.* 461 (2023) 141972, <https://doi.org/10.1016/j.cej.2023.141972>.
- [36] C. Liao, J. Zhu, Z. Cui, M. Gao, W. Wang, Q. Liu, R. Zou, Efficient trapping of lithium-ions by branched amine for stable lithium metal anodes, *Chem. Eng. J.* 487 (2024) 150667, <https://doi.org/10.1016/j.cej.2024.150667>.
- [37] M. Hu, Q. Ma, Y. Yuan, Y. Pan, M. Chen, Y. Zhang, D. Long, Grafting polyethyleneimine on electrospun nanofiber separator to stabilize lithium metal anode for Lithium sulfur batteries, *Chem. Eng. J.* 388 (2020) 124258, <https://doi.org/10.1016/j.cej.2020.124258>.
- [38] J. Vetter, P. Novak, M.R. Wagner, C. Veit, K.-C. Moller, J.O. Besenhard, M. Winter, M. Wohlfahrt-Mehrens, C. Vogler, A. Hammouche, Ageing mechanisms in lithium-ion batteries, *J. Power Sources* 147 (2005) 269–281, <https://doi.org/10.1016/j.jpowsour.2005.01.006>.
- [39] S. Park, G. Choi, H.Y. Lim, K.M. Jung, S.K. Kwak, N.-S. Choi, A Phosphorofluoridate-Based multifunctional electrolyte additive enables long cycling of high-energy lithium-ion batteries, *ACS Appl. Mater. Interfaces* 15 (2023) 33693–33702, <https://doi.org/10.1021/acsami.3c06882>.
- [40] C. Song, H. Moon, K. Baek, C. Shin, k. Lee, S.J. Kang, N.-S. Choi, Acid- and gas-scavenging electrolyte additive improving the electrochemical reversibility of Ni-Rich cathodes in Li-ion batteries, *ACS Appl. Mater. Interfaces* 15 (2023) 22157–22166, <https://doi.org/10.1021/acsami.3c02231>.
- [41] J.H. Ahn, H.-M. Kim, Y.-J. Lee, D. Esken, D. Dehe, H.A. Song, D.-W. Kim, Nanostructured reactive alumina particles coated with water-soluble binder on the polyethylene separator for highly safe lithium-ion batteries, *J. Power Sources* 506 (2021) 230119, <https://doi.org/10.1016/j.jpowsour.2021.230119>.
- [42] A.-H. Ban, S.-J. Pyo, W.J. Bae, H.-S. Woo, J. Moon, D.-W. Kim, Dual-type gel polymer electrolyte for high-voltage lithium metal batteries with excellent cycle life, *Chem. Eng. J.* 475 (2023) 146266, <https://doi.org/10.1016/j.cej.2023.146266>.
- [43] Y. Lee, T.K. Lee, S. Kim, J. Lee, Y. Ahn, K. Kim, H. Ma, G. Park, S.-M. Lee, S. K. Kwak, N.-S. Choi, Fluorine-incorporated interface enhances cycling stability of lithium metal batteries with Ni-rich NCM cathodes, *Nano Energy* 67 (2020) 104309, <https://doi.org/10.1016/j.nanoen.2019.104309>.
- [44] Y. Ruan, X. Song, Y. Fu, C. Song, V. Battaglia, Structural evolution and capacity degradation mechanism of $\text{LiNi}_{0.6}\text{Mn}_{0.2}\text{Co}_{0.2}\text{O}_2$ cathode materials, *J. Power Sources* 400 (2018) 539–548, <https://doi.org/10.1016/j.jpowsour.2018.08.056>.
- [45] H. Liu, M. Wolfman, K. Karki, Y.-S. Yu, E.A. Stach, J. Cabana, K.W. Chapman, P. J. Chupas, Intergranular cracking as a major cause of long-term capacity fading of layered cathodes, *Nano Lett.* 17 (2017) 3452–3457, <https://doi.org/10.1021/acs.nanolett.7b00379>.
- [46] D.-A. Lim, Y.-K. Shin, J.-H. Seok, D. Hong, K.H. Ahn, C.H. Lee, D.-W. Kim, *ACS Appl. Mater. Interfaces* 14 (2022) 54688–54697, <https://doi.org/10.1021/acsami.2c15685>.
- [47] A. Manthiram, J.C. Knight, S.-T. Myung, S.-M. Oh, Y.-K. Sun, Nickel-rich and lithium-rich layered oxide cathodes: progress and perspectives, *Adv. Energy Mater.* 6 (2016) 1501010, <https://doi.org/10.1002/aenm.201501010>.
- [48] C. Park, E. Lee, S.H. Kim, J.-G. Han, C. Hwang, S.H. Joo, K. Baek, S.J. Kang, S. K. Kwak, H.-K. Song, N.-S. Choi, Malonic-acid-functionalized fullerene enables the interfacial stabilization of Ni-rich cathodes in lithium-ion batteries, *J. Power Sources* 521 (2022) 230923, <https://doi.org/10.1016/j.jpowsour.2021.230923>.
- [49] R. Sim, L. Su, A. Dolocan, A. Manthiram, Delineating the impact of transition-metal crossover on solid-electrolyte interphase formation with ion mass spectrometry, *Adv. Mater.* 36 (2024) 2311573, <https://doi.org/10.1002/adma.202311573>.